

Supplementary Information: Real-time monitoring of aerosol particle formation from sulfuric acid vapor at elevated concentrations and temperatures

Daniel Becker^a, Jonas Heitland^a, Philip T. M. Carlsson^b, Jonas Elm^c, Tinja Olenius^d, Sophia Tödter^a, Amir Kharrazizadeh^a, and Thomas Zeuch^{a*}

^a*Universität Göttingen, Institut für Physikalische Chemie, Tammannstr. 6, 37077 Göttingen, Germany. *E-mail: tzeuch1@gwdg.de*

^b*Forschungszentrum Jülich GmbH, Wilhelm-Johnen-Straße, 52425 Jülich, Germany.*

^c*Aarhus University, Langelandsgade 140, 8000 Aarhus C, Denmark.*

^d*Swedish Meteorological and Hydrological Institute, Air Quality Research Unit, Folkborgsvägen 17, SE-601 76 Norrköping, Sweden.*

Within the scope of the following sections, we provide additional characteristics of the new experimental setup (see Section 1) and details for the simulation (see Section 2), which were applied to analyze the time- and size-dependent particle data.

1 Additional Information on the Experimental Setup, Particle Measurements and Data Treatment

1.1 Concentration of Trace Gases

The fraction of trace gases transported from premixing chambers to the reaction cell can either be calculated from the ideal gas law or calibrated by means of IR absorption.

From a known chamber volume $V_{\text{premix}} = 421$ and the pressure drop from $p_0 \approx 2.1$ bar to $p_1 \approx 1.3$ bar, one can calculate the total amount of carrier gas n_2 being transferred to the reaction cell:

$$n_2 = n_0 - n_1 \quad (\text{S1})$$

$$= (p_0 - p_1) \frac{V_{\text{premix}}}{RT} \quad (\text{S2})$$

$$= 1.356 \text{ mol} \quad (\text{S3})$$

Multiplication with the mole fraction gives the amount of pure trace substance. For example, filling 6.9 Pa of alkene in the premixing chamber would correspond to 69 ppm in case of a total pressure of 1 bar like it was used in the old setup, but due to the new filling pressure of 2.1 bar, the real mole fraction is only ≈ 32.9 ppm.

$$n_{2,\text{pure}} = 3.29 \times 10^{-5} \times 1.356 \text{ mol} \quad (\text{S4})$$

$$= 4.455 \times 10^{-5} \text{ mol} \quad (\text{S5})$$

Setting this into relation to the total amount of substance in the reaction cell, gives the new mole fraction.

$$x_{\text{reac.}} = \frac{n_{2,\text{pure}}}{n_{\text{tot, reac.}}} \quad (\text{S6})$$

$$= \frac{4.455 \times 10^{-5} \text{ mol}}{2.583 \text{ mol}} \quad (\text{S7})$$

$$= 1.725 \times 10^{-5} \quad (\text{S8})$$

We can now compare both mole fractions prior to and after the expansion, but have to refer to the same reference pressure of 1 bar and therefore take $x_{\text{premix.}}$ as 69 ppm.

$$f = \frac{x_{\text{reac.}}}{x_{\text{premix.}}} \quad (\text{S9})$$

$$= \frac{1.725 \times 10^{-5}}{6.9 \times 10^{-5}} \quad (\text{S10})$$

$$\approx 25 \% \quad (\text{S11})$$

The calculation shows that filling of 6.9 Pa into the premixing chamber leads to a final concentration of 18 ppm in the reaction cell at a pressure of 1 bar.

In a later campaign, we worked with formic acid and decided to use this compound for double checking the calculations above. HCOOH is a suitable trace substance for this purpose since it can be filled volumetrically as pure substance and has a strong IR absorption band. Thus, IR spectra for formic acid were recorded by either expanding from the premixing chamber or by direct filling into the cell. As depicted in Figure S1, integrated absorbance of two individual stretching modes show a linear correlation with the filled mole fraction. Integration of the C=O stretching mode $\nu_3^{[1]}$ was done from 1820 to 1723 cm^{-1} . The C-O stretching mode $\nu_6^{[1]}$ was integrated from 1148 to 1050 cm^{-1} .

To plot the corresponding data from the expansion method, the known mole

fractions from the premixing chamber were multiplied with the expected transport factor, thus giving different x-coordinates. Best agreement is achieved, if a transport factor of $27 \pm 1\%$ is assumed, confirming the calculation and also earlier work.

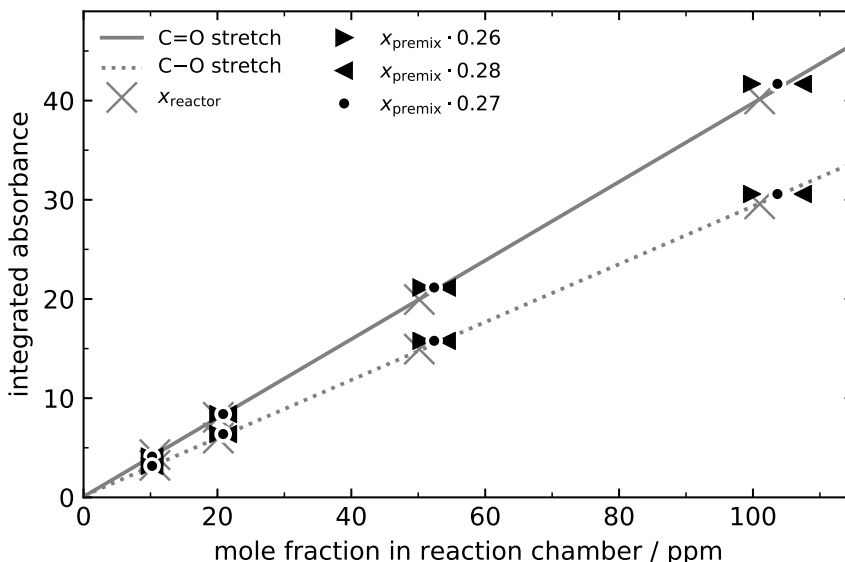


Figure S1: Calibration for estimating the fraction of transported trace gases from the premixing chamber to the reaction cell in a simultaneous expansion. The mole fraction in ppm refers to a total reaction cell pressure of 1 bar.

1.2 Time-Resolved Ozone-Spectra

As mentioned in the main text (see Fig. 2), ozone was used for monitoring the gas mixing. Figure S2 shows selected spectra of the full range (upper) and a zoomed view of the ν_3 band^[2] (lower), recorded during and after the expansion. The spectral resolution (spectrometer software setting) was 5 cm^{-1} , resulting in a sampling-time-resolution of 100 ms. Since the IR beam passes air outside of the reactor, water absorption is likely. We can reduce this by flushing the beam path with dried air, but we cannot completely suppress water bands. Of our used substances, butene has a broad IR absorption band at around 3000 cm^{-1} , where interferences from water signals occur. Contrastingly, ozone has two sharp bands in an undisturbed spectral range of which the ν_3 band is more intense. The maximum absorption found at 1055 cm^{-1} in the lower panel of Figure S2 is consistent with literature.^[3] However, during the expansion a shift of $\pm 1 \text{ cm}^{-1}$ is observed and linked to the spectrometers lower accuracy at very high scan rates.

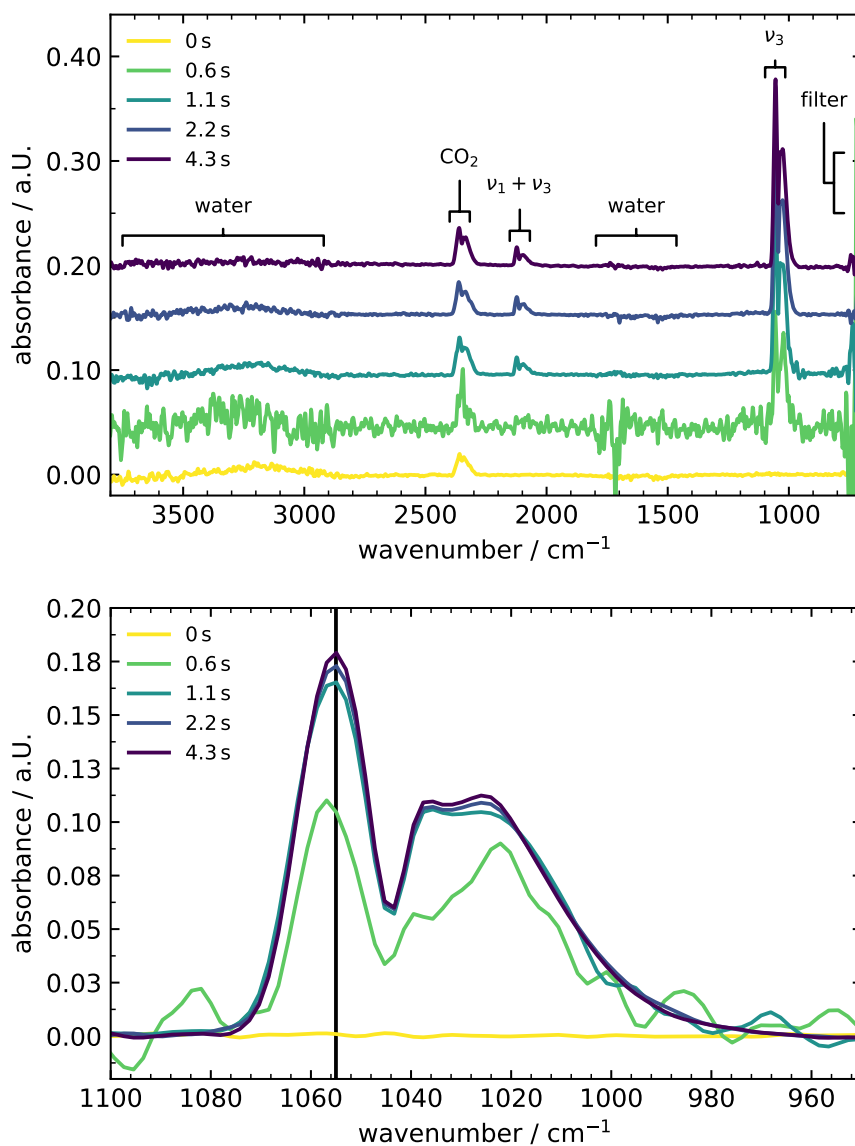


Figure S2: IR spectra of ozone at different times after opening of the valves. Upper: Full spectral range to demonstrate interference with ambient water. Arbitrary offsets were added for sake of visualization. Lower: Zoomed spectral range of the used ν_3 band.

1.3 Transport Time Correction

Collecting time-dependent data sets is not only governed by the system's dynamics, but may also be subject to the response of the used detection device. Especially for sampling with an SMPS, the transport from the chamber to the CPC must be taken into account and data correction is necessary.

To estimate the response of two SMPS devices in different configurations, a steady-state PSD was prepared from high amounts of H_2SO_4 and aged for several minutes. Since all fast dynamics were completed at this point (= static), the measured time delay of detection is completely determined by transport through tubing.

As depicted in Figure S3, the key parameter for reducing transport time is an enhanced sample flow rate, which is by far the highest for the 1 nm-SMPS working with the Nanoenhancer. The corresponding transport times ($t_{50\%}$) are listed in Table S1.

Table S1: Transport times of particles with $D_P = 30$ nm from the reactor to the detector. $t_{50\%}$ corresponds to the time at 50% of the signal height. In the case of the SMPS 3936, $t_{50\%}$ is the sum of transport time and an additional delay, in which the cell was filled manually to atmospheric pressure.

SMPS	Setup	Flow Rate / L min^{-1}	$t_{50\%}$ / s
TSI 1 nm-SMPS 3938E57	compact ^[4]	2.5	5.5
TSI 1 nm-SMPS 3938E57	standard	0.6	16.0
TSI 1 nm-SMPS 3938E57	standard	0.2	39.5
TSI SMPS 3936	standard	0.6	31.5
TSI SMPS 3936	standard	0.2	53.0

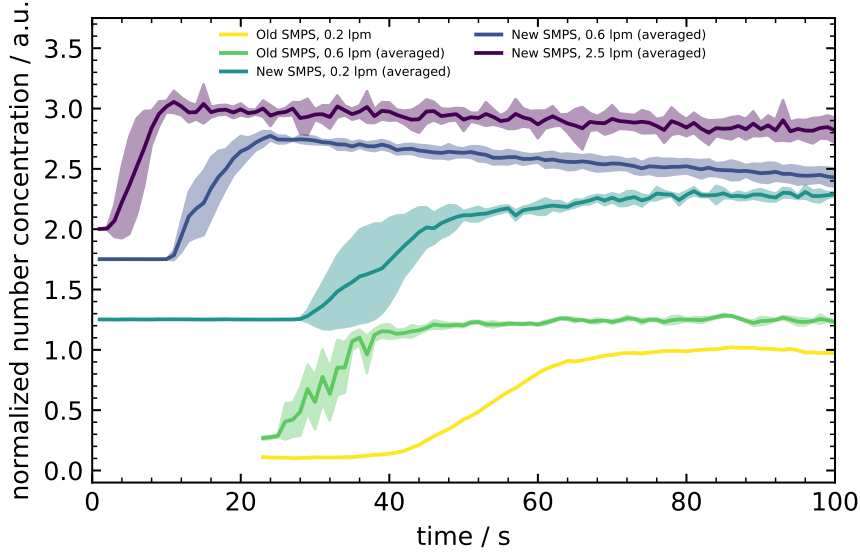


Figure S3: Estimation of transport times for two SMPS devices operated in different modes. Individual data sets were normalized to a maximum of 1 and averaged. The filled area corresponds to the standard deviation (1σ). For the estimation, times were read at 50% of signal height. For sake of an enhanced visibility, arbitrary offsets were added to the different data sets.

1.4 Diffusion Loss Correction

Measured concentration–time profiles of a single particle size class cover only a very narrow range of electrical mobility diameters, as shown in the next section. The diffusion loss in the signal is therefore approximately always the same in this interval. Furthermore, a correction is not required in this type of plots, because profiles were normalized to their maximum, as it is reported in the main text.

Contrastingly, when plotting PSD data as in sections 4.3 and 4.4 of the main text, diffusion losses should be taken into account, since absolute numbers from different particle diameters are compared here.

In the general correction procedure, the raw number concentrations of a PSD are divided by the total penetration efficiency P_{tot} , being the product of penetration through tubing P_{tube} and through parts of the SMPS P_{SMPS} .^[5] The latter are either included in the manufacturer’s software (Aerosol Instrument Manager 10.3 used for TSI SMPS 3936) or can be included in a post-processing fashion, when the new 1 nm-SMPS is operated in a compact design.^[5]

Losses in the external tubing are calculated using the following formulas taken from Soderholm.^[6]

$$P_{\text{tube}} = 1.0 - 5.499\mu_T^{2/3} + 3.770\mu_T + 0.8132\mu_T^{4/3}, \mu_T < 7.22 \times 10^{-3} \quad (\text{S12})$$

$$= 0.81905 \exp(-11.488\mu_T) + 0.09753 \exp(-70.072\mu_T) \quad (\text{S13})$$

$$+ 0.03250 \exp(-178.95\mu_T) + 0.01544 \exp(-338.10\mu_T),$$

$$\mu_T > 7.22 \times 10^{-3}$$

$$\mu_T = \frac{DL}{Q} \quad (\text{S14})$$

$$D = \frac{k_B T C_C}{3\pi\mu D_P} \quad (\text{S15})$$

The Cunningham slip correction factors, necessary to determine the particle diffusion coefficients, were interpolated from literature values.^[7]

Further quantities for calculations are provided in Table S2 and the overall penetration efficiencies for both SMPS operation modes are shown in Figure S4.

Table S2: Parameters necessary for calculation of P_{tube} .

Parameter	Meaning	Value
C_C	Cunningham slip correction	216 – 2.85
D_P	particle diameter	1.02 – 201.7 nm
μ	viscosity of air	18.5×10^{-5} Pa s
L	tube length	0.2 m (to new SMPS) 2.0 m (to old SMPS)
Q	sample flow rate	2.5 L min^{-1} (new SMPS) 0.2 L min^{-1} (old SMPS)
T	temperature	298 K

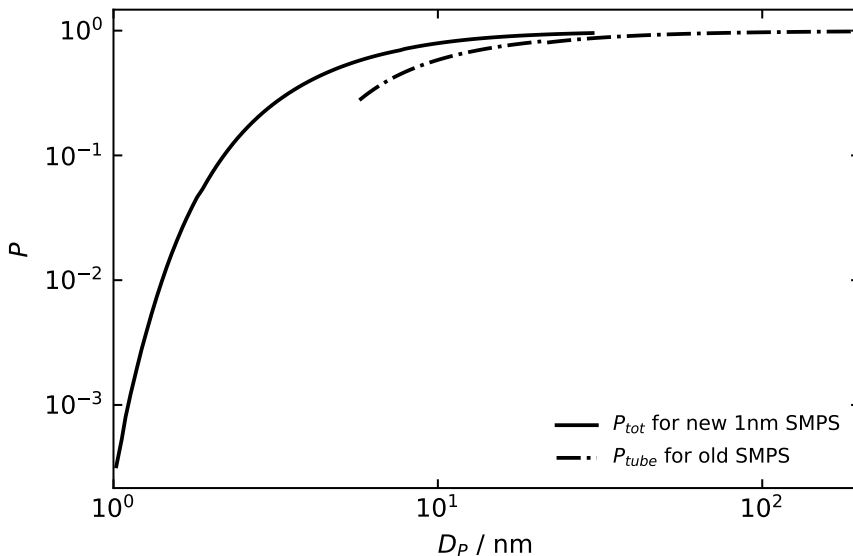


Figure S4: Calculated penetration efficiencies P_{tot} for the 1 nm-SMPS and P_{tube} for the old SMPS 3936. Because correction for 1 nm SMPS data was done in the post-processing way, P_{tot} is applied. For the SMPS 3936 losses inside the device were already corrected by TSI’s software (AIM 10.3) and therefore only tubing correction was necessary.

1.5 DMA Resolution

Setting a fixed voltage to the DMA’s center rod causes only particles within a narrow range of electrical mobility to pass through the exit slit. Such penetration is characterized by the transfer function Ω , having a triangular shape in the ideal case (assuming matching inlet and outlet flow, otherwise the shape is trapezoid-like).^[8,9] Since for small species diffusion must be taken into account again, we follow the work from Stolzenburg to calculate diffusion broadened transfer function^[9–11] based on a lognormal approximation. The results for the 1 nm-DMA operated at a sample flow of 2.5 l min^{-1} are nearly identical to that of the non-diffusion (ideal) scenario, for which the normalized/dimensionless electric mobility \tilde{Z}_P has values of 0.95 and 1.05 at the half maximum of Ω . For instance, calculations for the old SMPS’s NDMA (TSI Model 3085) showed significant broadening of the transfer function underlining the importance of upgrading to the new device. The corresponding diameter ranges for the 1 nm-DMA are given in Table S3.

1.6 Pressure Artifacts

As mentioned in the main text, artifacts were recognized in some runs of the experiment. They are only detected at the very beginning of data recording in a narrow time interval as shown in Figure S5. They are furthermore characterized by a steep rising edge, reaching an unphysical maximum of approx. 1600 cm^{-3} in this specific case (not shown). A possible explanation for this could be a

Table S3: Resolution of the 1 nm-DMA (TSI 3086) operated at nominal diameter (fixed voltage), a sample flow of 2.5 l min^{-1} and a sheath flow of 25 l min^{-1} . The upper and lower diameters were calculated from the corresponding minimal and maximal electrical mobilities at the half maximum of Ω .

$D_{\text{nominal}} / \text{nm}$	$D_{\text{min}} / \text{nm}$	$D_{\text{max}} / \text{nm}$
2.2	2.07	2.34
2.3	2.16	2.44
2.5	2.36	2.65
3.0	2.84	3.17
4.0	3.80	4.22
6.0	5.71	6.31
10.0	9.53	10.5
15.0	14.3	15.7
20.0	19.1	21.0
25.0	23.8	26.2
30.0	28.6	31.5

slight mismatch of reactor and ambient pressure. Even small differences, *e.g.*, in the range of approx. 20 mbar can then affect the SMPS's internal gas flow and trigger false counts on the CPC. The plots below also demonstrate that the raw signal at times $t > 10 \text{ s}$ is very reproducible. Furthermore, it is easy to classify the signal as an artifact and it is reasonable to neglect the peak in the upper trace.

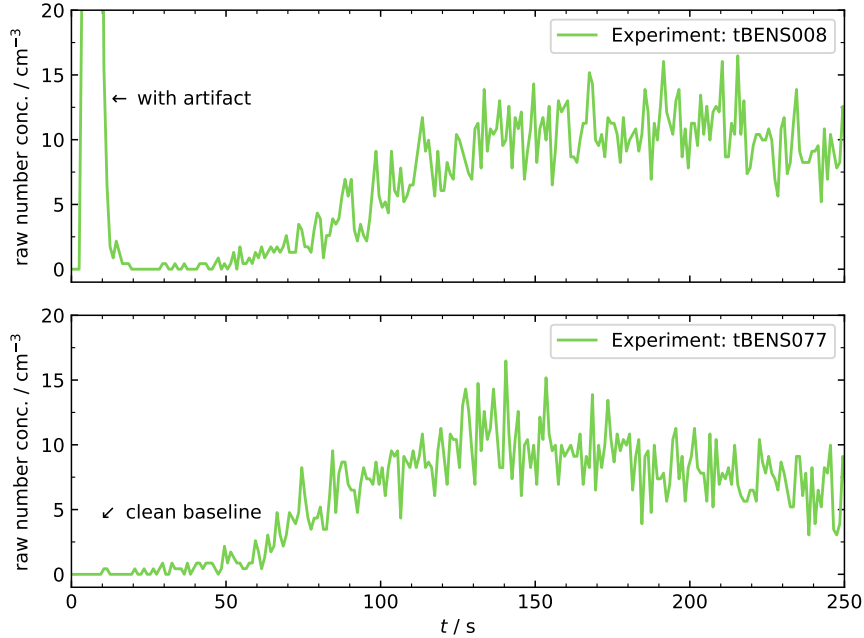


Figure S5: Raw concentration-time profiles for particles of $D_{\text{P}} = 3 \text{ nm}$ at an initial SO_2 concentration of 4.5 ppm. One of the traces has a significant artifact, whereas the second plot shows no particles at this time (as expected).

2 Additional Information on Theory and Kinetic Simulations

2.1 Quantum Chemical Calculations

The initial configurations of the $(\text{H}_2\text{SO}_4)_{2-5}$ clusters were obtained from the study of Kubečka *et al.*^[12] who used the following workflow:

ABCluster \rightarrow opt GFN-xTB \rightarrow low DFT opt \rightarrow high DFT opt \rightarrow high DFT freq \rightarrow DLPNO

Here ABOCluster refers to the initial global minimum search using a CHARMM forcefield with the ABOCluster program.^[13,14] In each step, geometry optimizations (opt) are performed using first an extended tight-binding method (GFN-xTB^[15]), followed by density functional theory using the ω B97X-D functional. Low and high refers to loose opt with a 6-31+G(d) basis set and default opt with a 6-31++G(d,p) basis set, respectively. Freq refers to a vibrational frequency calculation. In each step, redundant configurations are removed based on the radius of gyration, the energy, and the dipole moment, with the threshold of 0.01 Å, 0.001 E_{H} , and 0.1 D, respectively.

Here we undertook a slightly different approach. We took all the structures from the low DFT opt step (data obtained from^[12], at the courtesy of the authors) and fully re-optimized the structures and calculated vibrational frequencies at the ω B97X-D/6-31++G(d,p) level of theory. Redundant configurations were removed based on the root mean square deviation (RMSD) between atomic positions. This process will retain a larger pool of conformers compared to filtering out redundant configurations in each step. For each of the five cluster configurations lowest in free energy, high-level DLPNO-CCSD(T_0)^[16,17] single-point energy calculations were performed on top of the DFT structures. We employed an aug-cc-pVTZ basis set with the corresponding auxiliary basis sets /C and /JK for correlation and Coulomb/exchange fitting, respectively. We computed the DLPNO-CCSD(T_0) binding enthalpy as follows:

$$\Delta H_{\text{bind}}^{\text{DLPNO-CCSD}(T_0)} = \Delta E_{\text{bind}}^{\text{DLPNO-CCSD}(T_0)} + \Delta H_{\text{bind, thermal}}^{\omega\text{B97X-D}} \quad (\text{S16})$$

Here $\Delta E_{\text{bind}}^{\text{DLPNO-CCSD}(T_0)}$ is the electronic binding energy of the cluster and $\Delta H_{\text{bind, thermal}}^{\omega\text{B97X-D}}$ is the thermal contribution to the enthalpy. The entropy contributions are calculated based on the quasi-harmonic approximation^[18] using a 100 cm^{-1} cutoff. The free energy based on the quasi-harmonic approximation will be larger than in the corresponding harmonic approximation, as the vibrational entropy is reduced in this approach.^[19] The calculated thermochemistry is presented in Table S4.

2.2 Simulated Concentration-Time Profiles for H_2SO_4 and $(\text{H}_2\text{SO}_4)_2$

If direct measurements of condensable vapors *via* (Chemical Ionization) Atmospheric Pressure Interface Time-of-Flight Mass Spectrometry ((CI)-APi-TOF MS) is not possible, the evolution of H_2SO_4 over time can be calculated from

Table S4: Thermochemistry of the $(\text{H}_2\text{SO}_4)_{2-5}$ clusters, calculated at the DLPNO-CCSD(T_0)/aug-cc-pVTZ// ω B97X-D/6-31++G(d,p) level of theory using the quasi-harmonic approximation (298.15 K and 1 atm). The ΔH values are in kcal mol⁻¹ and ΔS is in cal mol⁻¹ K⁻¹.

Cluster	ΔH	ΔS
$(\text{H}_2\text{SO}_4)_2$	-17.768246	-40.565580
$(\text{H}_2\text{SO}_4)_3$	-33.960224	-78.885468
$(\text{H}_2\text{SO}_4)_4$	-55.449138	-129.633485
$(\text{H}_2\text{SO}_4)_5$	-77.003586	-176.144783

known gas phase kinetics and mixing ratios.^[20,21] Here, we used our kinetic model with literature rate coefficients and provide this additional information for five different mixing ratios of initial SO_2 mentioned in the main text. Direct measurements by mass spectrometry would be useful, but are not possible in the current setup. As can be seen in Figure S6, very high concentrations of sulfuric acid can be reached within a few seconds (For comparison: typical concentrations of H_2SO_4 are in the range of 10^5 – 10^6 cm⁻³ at clean sites (*e.g.*, Hyytiälä,^[22,23] Jungfraujoch^[24]) and up to $\approx 10^7$ cm⁻³ in urban areas (*e.g.*, Shanghai^[25]). Measurements performed at, *e.g.*, CLOUD Chamber range from 10^6 – 10^9 cm⁻³^[25]). Furthermore, the shape changes from sigmoidal to more peak-like, being in agreement with the measured particle-concentration profiles. The same trend can be observed for initial small clusters, *e.g.*, the sulfuric acid dimer as shown on the right hand side of Figure S6.

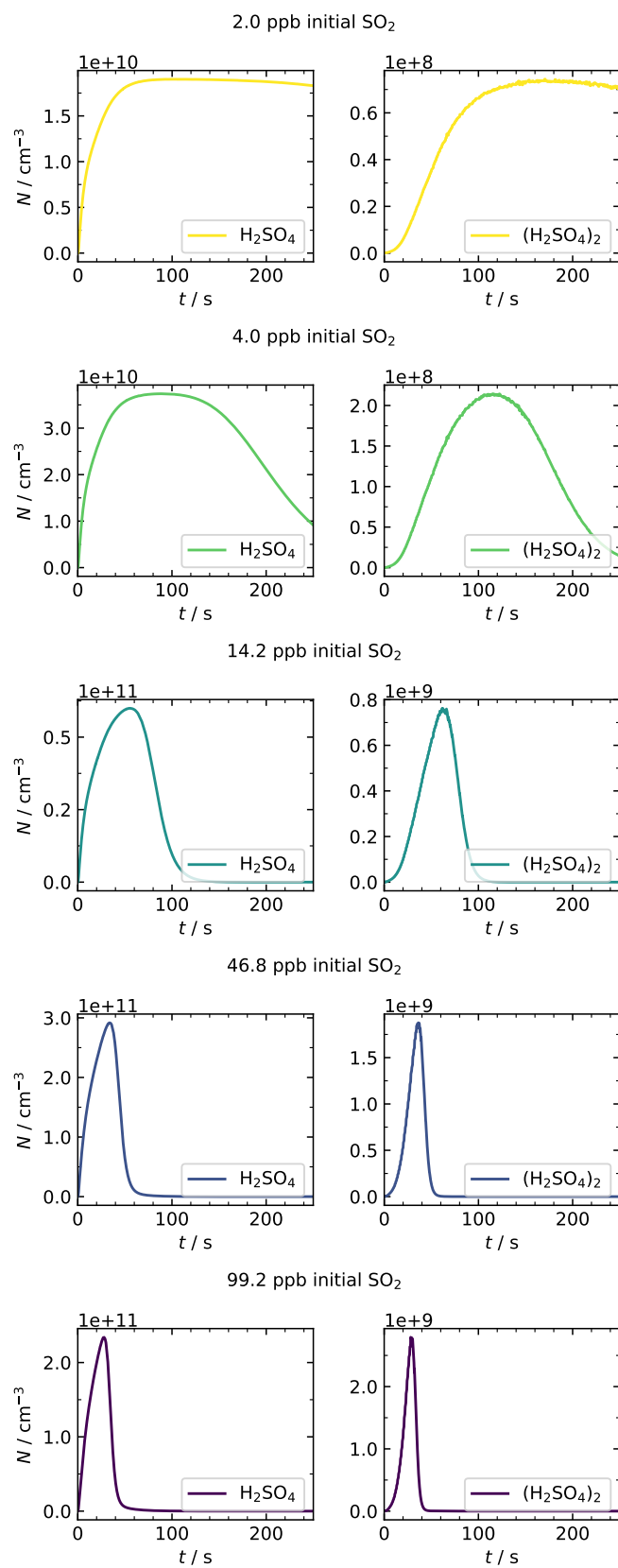


Figure S6: Simulated H₂SO₄⁻ and (H₂SO₄)₂⁻ profiles for various initial amounts of SO₂, 18 ppm butene and 0.8 ppm O₃.

References

- [1] M. Freytes, D. Hurtmans, S. Kassı, J. Liévin, J. V. Auwera, A. Campargue, M. Herman, “Overtone spectroscopy of formic acid”, *Chemical Physics* **2002**, *283*, 47–61, DOI 10.1016/s0301-0104(02)00507-4.
- [2] D. McCaa, J. Shaw, “The infrared spectrum of ozone”, *Journal of Molecular Spectroscopy* **1968**, *25*, 374–397, DOI 10.1016/s0022-2852(68)80050-5.
- [3] J. F. da Silveira Petrucci, P. R. Fortes, V. Kokoric, A. Wilk, I. M. Raimundo, A. A. Cardoso, B. Mizaikoff, “Real-time monitoring of ozone in air using substrate-integrated hollow waveguide mid-infrared sensors”, *Scientific Reports* **2013**, *3*, DOI 10.1038/srep03174.
- [4] Diffusion Correction Using TSI’s 1 nm SMPS System Model 3938, Application Note, **2019**.
- [5] Aerosol Instrument Manager Software For Scanning Mobility Particle Size (SMPS) Spectrometers, TSI, **2018**.
- [6] S. C. Soderholm, “Analysis of diffusion battery data”, *Journal of Aerosol Science* **1979**, *10*, 163–175, DOI 10.1016/0021-8502(79)90065-x.
- [7] J. H. Seinfeld, S. N. Pandis, *Atmospheric Chemistry and Physics*, John Wiley & Sons Inc, **2006**, ISBN: 1118947401.
- [8] E. Knutson, K. Whitby, “Aerosol classification by electric mobility: apparatus, theory, and applications”, *Journal of Aerosol Science* **1975**, *6*, 443–451, DOI 10.1016/0021-8502(75)90060-9.
- [9] M. R. Stolzenburg, P. H. McMurry, “Equations Governing Single and Tandem DMA Configurations and a New Lognormal Approximation to the Transfer Function”, *Aerosol Science and Technology* **2008**, *42*, 421–432, DOI 10.1080/02786820802157823.
- [10] M. R. Stolzenburg, PhD thesis, University of Minnesota, **1988**.
- [11] M. R. Stolzenburg, “A review of transfer theory and characterization of measured performance for differential mobility analyzers”, *Aerosol Science and Technology* **2018**, *52*, 1194–1218, DOI 10.1080/02786826.2018.1514101.
- [12] J. Kubečka, V. Besel, T. Kurtén, N. Myllys, H. Vehkamäki, “Configurational sampling of noncovalent (atmospheric) molecular clusters: Sulfuric acid and guanidine”, *J. Phys. Chem. A* **2019**, *123*, 6022–6033.
- [13] J. Zhang, M. Dolg, “ABCcluster: the artificial bee colony algorithm for cluster global optimization”, *Phys. Chem. Chem. Phys.* **2015**, *17*, 24173–24181.
- [14] J. Zhang, M. Dolg, “Global optimization of clusters of rigid molecules using the artificial bee colony algorithm”, *Phys. Chem. Chem. Phys.* **2016**, *18*, 3003–3010.
- [15] S. Grimme, C. Bannwarth, P. Shushkov, “A Robust and Accurate Tight-Binding Quantum Chemical Method for Structures, Vibrational Frequencies, and Noncovalent Interactions of Large Molecular Systems Parametrized for All spd-Block Elements ($Z = 1-86$)”, *J. Chem. Theory Comput.* **2017**, *13*, 1989–2009.

- [16] C Riplinger, F Neese, “An Efficient and Near Linear Scaling Pair Natural Orbital Based Local Coupled Cluster Method”, *J. Chem. Phys.* **2013**, *138*, 034106.
- [17] C Riplinger, B Sandhoefer, A Hansen, F Neese, “Natural Triple Excitations in Local Coupled Cluster Calculations with Pair Natural Orbitals”, *J. Chem. Phys.* **2013**, *139*, 134101.
- [18] S. Grimme, “Supramolecular Binding Thermodynamics by Dispersion-corrected Density Functional Theory”, *Chem. Eur. J.* **2012**, *18*, 9955–9964.
- [19] N. Myllys, J. Elm, T. Kurtén, “Density functional theory basis set convergence of sulfuric acid-containing molecular clusters”, *Computational and Theoretical Chemistry* **2016**, *1098*, 1–12, DOI 10.1016/j.comptc.2016.10.015.
- [20] T. Berndt, O. Böge, F. Stratmann, J. Heintzenberg, M. Kulmala, “Rapid Formation of Sulfuric Acid Particles at Near-Atmospheric Conditions”, *Science* **2005**, *307*, 698–700, DOI 10.1126/science.1104054.
- [21] A. Metzger, B. Verheggen, J. Dommen, J. Duplissy, A. S. H. Prevot, E. Weingartner, I. Riipinen, M. Kulmala, D. V. Spracklen, K. S. Carslaw, U. Baltensperger, “Evidence for the role of organics in aerosol particle formation under atmospheric conditions”, *Proceedings of the National Academy of Sciences* **2010**, *107*, 6646–6651, DOI 10.1073/pnas.0911330107.
- [22] V.-M. Kerminen, T. Petäjä, H. E. Manninen, P. Paasonen, T. Nieminen, M. Sipilä, H. Junninen, M. Ehn, S. Gagné, L. Laakso, I. Riipinen, H. Vehkamäki, T. Kurten, I. K. Ortega, M. D. Maso, D. Brus, A. Hyvärinen, H. Lihavainen, J. Leppä, K. E. J. Lehtinen, A. Mirme, S. Mirme, U. Hörrak, T. Berndt, F. Stratmann, W. Birmili, A. Wiedensohler, A. Metzger, J. Dommen, U. Baltensperger, A. Kiendler-Scharr, T. F. Mentel, J. Wildt, P. E. W. P. M. Winkler and, A. Petzold, A. Minikin, C. Plass-Dülmer, U. Pöschl, A. Laaksonen, M. Kulmala, “Atmospheric nucleation: highlights of the EUCAARI project and future directions”, *Atmos. Chem. Phys. Discuss.* **2010**, *10*, 16497–16549.
- [23] T. Petäjä, I. R. L. Mauldin, E. Kosciuch, J. McGrath, T. Nieminen, P. Paasonen, M. Boy, A. Adamov, T. Kotiaho, M. Kulmala, “Sulfuric acid and OH concentrations in a boreal forest site”, *Atmospheric Chemistry and Physics* **2009**, *9*, 7435–7448, DOI 10.5194/acp-9-7435-2009.
- [24] F. Bianchi, J. Tröstl, H. Junninen, C. Frege, S. Henne, C. R. Hoyle, U. Molteni, E. Herrmann, A. Adamov, N. Bukowiecki, X. Chen, J. Duplissy, M. Gysel, M. Hutterli, J. Kangasluoma, J. Kontkanen, A. Kürten, H. E. Manninen, S. Münch, O. Peräkylä, T. Petäjä, L. Rondo, C. Williamson, E. Weingartner, J. Curtius, D. R. Worsnop, M. Kulmala, J. Dommen, U. Baltensperger, “New particle formation in the free troposphere: A question of chemistry and timing”, *Science* **2016**, *352*, 1109–1112, DOI 10.1126/science.aad5456.

- [25] L. Yao, O. Garmash, F. Bianchi, J. Zheng, C. Yan, J. Kontkanen, H. Junninen, S. B. Mazon, M. Ehn, P. Paasonen, M. Sipilä, M. Wang, X. Wang, S. Xiao, H. Chen, Y. Lu, B. Zhang, D. Wang, Q. Fu, F. Geng, L. Li, H. Wang, L. Qiao, X. Yang, J. Chen, V.-M. Kerminen, T. Petäjä, D. R. Worsnop, M. Kulmala, L. Wang, “Atmospheric new particle formation from sulfuric acid and amines in a Chinese megacity”, *Science* **2018**, *361*, 278–281, DOI [10.1126/science.aao4839](https://doi.org/10.1126/science.aao4839).